Monthly Notices
of the
ROYAL ASTRONOMICAL SOCIETY

MNRAS **446,** 3346–3355 (2015) doi:10.1093/mnras/stu2311

The density structure of the L1157 molecular outflow★†

A. I. Gómez-Ruiz,[1‡¶] C. Codella,[1] B. Lefloch,[2,3] M. Benedettini,[4] G. Busquet,[5,4] C. Ceccarelli,[2,3] B. Nisini,[6] L. Podio[1] and S. Viti[7]

[1]*INAF, Osservatorio Astrofisico di Arcetri, Largo E. Fermi 5, I-50125 Firenze, Italy*
[2]*Univ. Grenoble Alpes, IPAG, F-38000 Grenoble, France*
[3]*CNRS, IPAG, F-38000 Grenoble, France*
[4]*INAF, Istituto di Astrofisica e Planetologia Spaziali, via Fosso del Cavaliere 100, I-00133 Roma, Italy*
[5]*Instituto de Astrofísica de Andalucía, CSIC, Glorieta de la Astronomía s/n, E-18008 Granada, Spain*
[6]*INAF, Osservatorio Astronomico di Roma, via di Frascati 33, I-00040 Monte Porzio Catone, Italy*
[7]*Department of Physics and Astronomy, University College London, WC1E 6BT London, UK*

Accepted 2014 October 30. Received 2014 October 28; in original form 2014 May 22

ABSTRACT

We present a multiline CS survey towards the brightest bow-shock B1 in the prototypical chemically active protostellar outflow L1157. We made use of (sub-)mm data obtained in the framework of the Chemical HErschel Surveys of Star forming regions and Astrochemical Surveys at IRAM (ASAI) key science programs. We detected $^{12}C^{32}S$, $^{12}C^{34}S$, $^{13}C^{32}S$, and $^{12}C^{33}S$ emissions, for a total of 18 transitions, with E_u up to ∼180 K. The unprecedented sensitivity of the survey allows us to carefully analyse the line profiles, revealing high-velocity emission, up to 20 km s^{-1} with respect to the systemic. The profiles can be well fitted by a combination of two exponential laws that are remarkably similar to what previously found using CO. These components have been related to the cavity walls produced by the ∼2000 yr B1 shock and the older (∼4000 yr) B2 shock, respectively. The combination of low- and high-excitation CS emission was used to properly sample the different physical components expected in a shocked region. Our CS observations show that this molecule is highlighting the dense, n_{H_2} = 1–5 × 10^5 cm^{-3}, cavity walls produced by the episodic outflow in L1157. In addition, the highest excitation ($E_u \geq 130$ K) CS lines provide us with the signature of denser (1–5 × 10^6 cm^{-3}) gas, associated with a molecular reformation zone of a dissociative *J*-type shock, which is expected to arise where the precessing jet impacting the molecular cavities. The CS fractional abundance increases up to ∼10^{-7} in all the kinematical components. This value is consistent with what previously found for prototypical protostars and it is in agreement with the prediction of the abundances obtained via the chemical code Astrochem.

Key words: molecular data – stars: formation – ISM: molecules – radio lines: ISM – submillimetre: ISM.

1 INTRODUCTION

Bipolar fast jets driven by protostars are present during the earliest stages of low-mass star formation. The interaction of the jets with the high-density ambient medium creates shocks, which in turn trigger endothermic chemical reactions and ice grain mantle sublimation or sputtering. The chemical composition of the gas phase is consequently altered and enriched. One of the best studied protostellar outflows with strong shocks and very active chemistry is the bipolar outflow driven by the low-mass Class 0 protostar L1157-mm, located at a distance of ≃250 pc (Looney, Tobin & Kwon 2007), and with a luminosity of $L_{bol} \sim 3\,L_\odot$ (Tobin et al. 2010). Several blue- and red-shifted shocks have been revealed using CO (Gueth et al. 1996, 1998) and H_2 (Neufeld et al. 2009; Nisini et al. 2010). The interferometric CO maps made of this outflow showed that the spatial-kinematic structure of the blue lobe is reproduced by a model of two limb-brightened cavities with slightly different axes (Gueth, Guilloteau & Bachiller 1996). In particular, the shocks that produced the two cavities in the blue lobe were labelled B2 and B1 (with kinematical ages of ∼4000 and 2000 yr, respectively), of

★Based on observations carried out with *Herschel*. *Herschel* is an ESA space observatory with science instruments provided by European-led Principal Investigator consortia and with important participation from NASA.
†Based on observations carried out with the IRAM 30m Telescope. IRAM is supported by INSU/CNRS (France), MPG (Germany) and IGN (Spain).
‡E-mail: aigomez@inaoep.mx
¶Current address: Instituto Nacional de Astrofí,sica, Óptica y Electrónica (INAOE), Luis Enrique Erro No.1, C.P. 72840, Tonantzintla, Puebla, Mexico.

Table 1. CS critical densities, n_{cr}, for typical kinetic temperature of 60 K.

Transition	A_{ij} (s^{-1})	C_{ij} (cm^3 s^{-1})	n_{cr} (cm^{-3})
2–1	1.679E−05	4.35E−11	3.85E+05
3–2	6.071E−05	5.00E−11	1.21E+06
5–4	2.981E−04	5.42E−11	5.50E+06
6–5	5.230E−04	5.52E−11	9.47E+06
7–6	8.395E−04	5.64E−11	1.48E+07
10–9	2.496E−03	6.15E−11	4.05E+07
11–10	3.336E−03	6.35E−11	5.25E+07
12–11	4.346E−03	6.58E−11	6.60E+07

Note: A_{ij} coefficients and collisional rates (C_{ij}) from LAMDA data base (http://home.strw.leidenuniv.nl/~moldata/CS.html). The C_{ij} are for CS-H2, scaled from CS-He (Lique et al. 2006).

which B1 has been found to dominate the emission of several molecular transitions (Tafalla & Bachiller 1995; Zhang et al. 1995; Gueth, Guilloteau & Bachiller 1998; Zhang, Ho & Wright 2000; Bachiller et al. 2001). Interferometric observations have revealed the complex structure of the B1 shock, consisting of multiple clumps (Benedettini et al. 2007; Codella et al. 2009; Gómez-Ruiz et al. 2013) and characterized by an east–west chemical stratification (Benedettini et al. 2007, 2013). The B1 and B2 positions of the L1157 outflow have been the target of multiple molecular line studies that establish L1157 as the prototype of chemically active outflows (Bachiller & Perez Gutierrez 1997; Bachiller et al. 2001).

Under the framework of the IRAM Large Program ASAI[1] (Astrochemical Surveys at IRAM) and the Herschel key project CHESS [2] (Chemical HErschel Surveys of Star forming regions; Ceccarelli et al. 2010), an unbiased spectral line survey of the L1157-B1 position has been carried out in the range 80–350 GHz (with the IRAM-30m antenna) and 500–2000 GHz (with *Herschel*-Heterodyne Instrument for the Far-Infrared (HIFI)). The first results of the CHESS program (Codella et al. 2010, 2012a,b, 2013; Lefloch et al. 2010, 2012; Benedettini et al. 2012; Busquet et al. 2014) confirmed the chemical richness of the shocked gas, showing bright emission due to species released by grain mantles, such as NH_3, H_2O, and CH_3OH. In addition, we found that all the CO lines profiles are well fitted by a linear combination of three exponential laws of the form $I(v) = \exp\ -\ |v/v_0|$, which trace three different kinematical and thermal components. These components are (i) a molecular reformation region of a dissociative J-shock occurring at the B1 position (also refereed as g_1; Lefloch et al. 2012), (ii) the B1 cavity wall (g_2), and (iii) the older B2 cavity (g_3). For each component the CO molecule has provided severe constrains of the kinetic temperature, $T_k \sim 210$, 64, and 23 K, respectively, whereas only lower limits of the gas density have been provided.

The CS molecule can fix the density uncertainty, given (i) it is a standard density tracer (van der Tak et al. 2007), due to the high critical density of most of the transitions (see Table 1), i.e. subthermal excitation, and (ii) the CS abundance, X(CS), in shocked material along molecular outflows (e.g. Bachiller et al. 2001; Wakelam et al. 2005; Tafalla et al. 2010) increases up to an order of magnitude with respect to what observed in quiescent clouds. Indeed CS can be efficiently formed from species such as OCS, that together with H_2S is the most abundant S-bearing molecule released from the grain mantles after a shock, and injected into the gas phase (Wakelam et al. 2004, 2005; Codella et al. 2005). This hypothesis is supported by recent results on molecular ions by Podio et al. (2014), who found that if OCS is released from dust grains it is possible to simultaneously reproduce the CS and HCS^+ abundances. The CS emission can thus be used to characterize the physical conditions of the gas components in L1157-B1 as revealed by CO. Only the combination of low-J CS lines observed with IRAM and the high-J CS lines observed with *Herschel*-HIFI can properly sample the different physical components that may compose the line profiles. The observations are reported in Section 2, while in Section 3 we describe the line profiles and their decomposition into different components; the physical conditions and the derived CS abundances are reported in Section 4. Our conclusions are summarized in Section 5.

2 OBSERVATIONS

2.1 *Herschel*-HIFI

The CS(10–9), (11–10), (12–11) transitions were observed with *Herschel*-HIFI on 2010 October 27 and 2009 August 1 (Obs_ID 1342207575 and 1342181160), during the unbiased spectral survey CHESS with the HIFI bands 1a and 1b, at the position of the B1 shock in L1157 (see Fig. 1). The pointed coordinates were $\alpha_{2000} = 20^h39^m10\overset{s}{.}2$, $\delta_{J2000} = +68°01'10\overset{''}{.}5$, i.e. at $\Delta\alpha = +25\overset{''}{.}6$ and $\Delta\delta = -63\overset{''}{.}5$ from the driving protostar. The receiver was tuned in double side band mode, with a total integration time of 8912 and 8400 s to cover bands 1a and 1b, respectively. The Wide Band Spectrometer was used, with a velocity resolution of 0.15–0.17 km s^{-1}, depending on frequency. All HIFI spectra were smoothed to a common velocity resolution of 1.4 km s^{-1}, in order to be compared with the IRAM-30m spectra (see below). The forward (F_{eff}) and beam (B_{eff}) efficiencies, as well as the Half Power Beam Width (HPBW) were taken according to Roelfsema et al. (2012) and reported in Table 2.[3] The *Herschel* data were processed with the ESA-supported package HIPE 8.1[4] (Herschel Interactive Processing Environment: Ott 2010). FITS files from level 2 were then created and transformed into GILDAS[5] format for data analysis. The CS (13–12) at 636532.454 MHz falls right at the outer edge of band 1b and was missed by our HIFI/CHESS survey. The CS (14–13) at 685435.917 MHz lies in band 2a and was observed (Obs_ID:1342207607), but not detected down to an rms of 3.6 mK [Ta*] in a velocity interval of 5 km s^{-1}. Therefore, the HIFI/CHESS survey detected the CS transitions from $J_{up} = 10$ up to the $J_{up} = 12$.

2.2 IRAM-30m

The lower$J$ CS transitions ($J_{up} = 2$, 3, 5, 6, 7) were obtained during the IRAM-30m unbiased spectral survey of L1157-B1 (Lefloch et al., in preparation) as part of the ASAI Large Program towards the same position observed with *Herschel*-HIFI. The survey was performed during several runs in 2011 and 2012, using the broad-band Eight MIxer Receiver (EMIR) instrument,

[1] PI: Bachiller/Lefloch. http://www.oan.es/asai
[2] PI: Ceccarelli. http://chess.obs.ujf-grenoble.fr

[3] The data presented here do not include the updated HIFI calibration values as of 2014 September 26. However, this does not affect significantly the main results of our analysis.
[4] HIPE is a joint development by the Herschel Science Ground Segment Consortium, consisting of ESA, the NASA Herschel Science Center, and the HIFI, PACS, and SPIRE consortia.
[5] http://iram.fr/IRAMFR/PDB/gildas/gildas.html

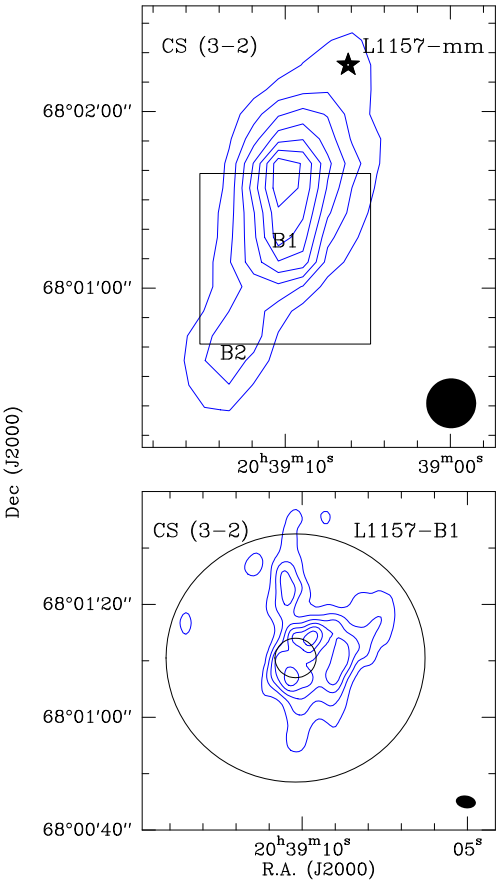

Figure 1. The CS(3–2) emission integrated from ∼−21 to +5 km s^{-1} in the blue lobe of the L1157 outflow. Upper panel: IRAM 30-m single-dish map of the blue lobe (first contour and steps of 3 K km s^{-1}, corresponding to ∼3σ). The star points out the position of the driving protostar L1157-mm. The labels indicate the main blue-shifted knots B1 and B2. The ellipse in the bottom-right corner shows the HPBW. Lower panel: IRAM PdBI CS(3–2) image (the synthesized beam is reported in the bottom-right corner) of the B1 clump (Benedettini et al. 2013; first contour and steps of 0.5 Jy beam^{-1} km s^{-1}, corresponding to ∼3σ). Circles are for the smallest (7 arcsec) and largest (44 arcsec) HPBW of the present data set.

the Fourier Transform Spectrometer (FTS; velocity resolution up to 1.4 km s^{-1}) and the Wideband Line Multiple Autocorrelator (WILMA) spectrometer (only the 6–5 transitions; ∼2.1 km s^{-1}). All the spectra taken with the FTS were smoothed to a common velocity resolution of 1.4 km s^{-1}. The forward and beam efficiencies, as well as the HPBW are reported in Table 2. As complementary data, the CS(3–2) line emission was mapped at the Nyquist spatial frequency (i.e. every 8 arcsec) in a region of ∼200 arcsec × 400 arcsec, covering the entire blue lobe of the L1157 outflow in 2011 September with the IRAM-30m antenna (see Fig. 1, upper panel). The spectral resolution was 0.4 km s^{-1}. The average rms of the map was ∼0.1 K per velocity interval.

The total frequency coverage of the survey allow us to observe most of the CS rotational transitions from J = 2–1 up to J = 12–11, as well as some isotopic species transitions (in particular low-J transitions). We did not observe the J = 1–0, 4–3, 8–7, and 9–8 transitions. The spectra in this paper are reported in units of main-beam brightness temperature ($T_{\rm MB} = T_A^* \times F_{\rm eff}/B_{\rm eff}$), for which we have used the $F_{\rm eff}$ and $B_{\rm eff}$ in Table 2. Nominal flux calibration uncertainties of 10 and 20 per cent, for Herschel and IRAM-30m, respectively, are considered in the analysis.

3 RESULTS

3.1 Detected transitions and line opacities

The observed transitions of CS and its isotopologues are listed in Table 2. In total 18 transitions from ^{12}CS, ^{13}CS, C^{33}S, and C^{34}S were detected. In Table 2 are reported the peak intensities ($T_{\rm MB}^{\rm peak}$), the velocity limits of the detection ($V_{\rm min}$ and $V_{\rm max}$, defined at a 3σ detection limit), and the integrated emission within this limits ($\int T_{\rm MB} {\rm d}v$). Figs 2 and 3 show the spectra of the CS and its isotopologues transitions, respectively. The strongest lines are CS (2–1) and (3–2), with typical peak intensities between ∼2–3 K. The highest velocities detected in these transitions reach up to $V_{\rm LSR} \sim -20$ km s^{-1} (cloud velocity is $V_{\rm sys} = +2.6$ km s^{-1}: e.g. Bachiller & Perez Gutierrez 1997). On the other hand, the highest frequency lines observed with HIFI have typical peak intensities of ∼30–60 mK, and they span a much narrow velocity range, with the highest velocity up to $V_{\rm LSR} \sim -5$ km s^{-1}. The isotopologues were detected up to the J = 6–5 transition, with peak intensities in the 20–160 mK range.

Since only the 2–1 line of all the isotopologues was detected in a wide range of velocities with a good signal-to-noise ratio (i.e. >4), we use it to determine the CS (2–1) line opacity as a function of velocity. For this aim, we assumed the following abundance ratios: ^{12}C/^{13}C=75, ^{32}S/^{34}S=22, ^{32}S/^{33}S=138 (Wilson & Rood 1994; Chin et al. 1996). Fig. 4 shows the opacity the CS (2–1) transition as a function of velocity, obtained from the C^{32}S/C^{34}S and ^{12}CS/^{13}CS ratios. We found $\tau \sim 0.05$ at $V_{\rm LSR}$ of −7.5 km s^{-1} (the highest velocity in which the line ratio is >2σ), while $\tau \sim 1$ at the cloud velocity. With these information, we conclude that the CS emission is at most moderately optically thick (i.e. $\tau < 2$), and at the outflow velocities ($V_{\rm LSR} < -6$ km s^{-1}) there is evidence for optically thin CS emission. Fig. 4 also shows the excitation temperature ($T_{\rm ex}$–$T_{\rm bg}$), uncorrected for beam filling (ff), and as a function of velocity (discussed in Section 4).

The IRAM-30m CS (3–2) map integrated between $V_{\rm LSR}$ of −21 to +5 km s^{-1}, shown in Fig. 1, traces the large-scale CS gas structure of B1 and B2, being consistent with previous results by Bachiller et al. (2001). As shown by Benedettini et al. (2013), the interferometric data recovers most of the emission at the highest negative velocities (100 per cent at $V_{\rm LSR} < -6$ km s^{-1}), while it loses a considerable fraction of the emission (∼40 per cent) around the cloud velocity (see Benedettini et al. 2013 for details). Thus, the total integrated emission observed in the interferometric map shown in the lower panel of Fig. 1 is dominated by the high-velocity structures. As shown below, the information provided by this map will allow us to constrain the physical conditions obtained from our multiline CS analysis.

3.2 CS spectral line components

Thanks to the high signal-to-noise ratio of the ASAI data, we have analysed the profiles of the CS transitions from J = 2–1 up to J = 7–6 following the approach of Lefloch et al. (2012). Fig. 5 shows the line profiles of the CS transitions J = 2–1 up to J = 7–6 on a linear-logarithmic scale. We identify two physical components, whose intensity–velocity distributions can be fitted with an exponential law $I(v) \propto \exp(-|v/v_0|)$ with the same slope at all J, but differing relative intensities.

Table 2. Transitions, parameters, and integrated intensities of the CS and isotopologues lines observed.

Transition[a]	ν_0 (GHz)	E_u (K)	Telescope	HPBW (arcsec)	B_{eff}	F_{eff}	T_{MB}^{peak} [b] (K)	V_{min}, V_{max} (km s^{-1})	$\int T_{MB} dv$[d] (K km s^{-1})
				$^{12}C^{32}S$					
2–1	97.980 95	7	IRAM	26	0.80	0.95	2.45(0.002)	−19, 6	17.28
3–2	146.969 03	14	IRAM	17	0.74	0.93	2.96(0.004)	−19, 6	21.03
5–4	244.935 56	35	IRAM	10	0.56	0.94	2.34(0.004)	−16, 6	17.62
6–5	293.91209	49	IRAM	9	0.45	0.88	1.61(0.006)	−16, 6	12.67
7–6	342.882 85	65	IRAM	7	0.35	0.82	0.96(0.026)	−16, 3	7.40
10–9	489.751 04	129	HIFI	44	0.73	0.96	0.06(0.008)	−4, 3	0.38
11–10	538.689 00	155	HIFI	39	0.73	0.96	0.04(0.006)	−5, 3	0.34
12–11	587.616 49	183	HIFI	36	0.72	0.96	0.03(0.009)	−3, 4	0.25
				$^{12}C^{34}S$					
2–1	96.412 95	7	IRAM	26	0.80	0.95	0.15(0.001)	−14, 4	1.12
3–2	144.617 10	14	IRAM	17	0.74	0.93	0.16(0.002)	−13, 4	1.16
5–4	241.016 08	35	IRAM	10	0.57	0.94	0.11(0.003)	−10, 4	0.77
6–5	289.209 07	49	IRAM	9	0.46	0.88	0.05(0.007)	−7, 3	0.39
7–6	337.396 45	50	IRAM	7	0.35	0.82	<0.08[c]	–	–
10–9	481.915 86	96	HIFI	44	0.73	0.96	<0.05[c]	–	–
11–10	530.071 22	115	HIFI	40	0.73	0.96	<0.05[c]	–	–
12–11	578.216 05	135	HIFI	37	0.72	0.96	<0.05[c]	–	–
				$^{13}C^{32}S$					
2–1	92.494 30	7	IRAM	26	0.80	0.95	0.05(0.002)	−15, 5	0.34
3–2	138.739 33	13	IRAM	17	0.74	0.93	0.06(0.003)	−11, 4	0.43
5–4	231.220 99	33	IRAM	10	0.58	0.94	0.03(0.003)	−10, 4	0.25
6–5	277.455 40	47	IRAM	9	0.46	0.88	<0.02[c]	–	–
11–10	508.528 14	146	HIFI	42	0.73	0.96	<0.03[c]	–	–
				$^{12}C^{33}S$					
2–1	97.172 06	6	IRAM	26	0.80	0.95	0.02(0.002)	−11, 4	0.15
3–2	145.155 53	12	IRAM	17	0.74	0.93	0.03(0.003)	−7, 4	0.25
5–4	242.913 61	28	IRAM	10	0.56	0.94	0.02(0.004)	−7, 3	0.12
6–5	291.485 93	39	IRAM	9	0.46	0.88	<0.02[c]	–	–

Notes: [a]Transition properties are taken from the Cologne Database for Molecular Spectroscopy: Müller et al. (2005). [b]In parenthesis the rms (σ) per channel width (Δv) of 1.4 km s^{-1}, except for the 6–5 lines with $\Delta v \sim 2.1$ km s^{-1}. [c]3σ upper limit. [d]The integrated area between V_{min}, V_{max} (see Section 3.1).

For $J = 6$–5 and $J = 7$–6, the intensity–velocity distribution in the line profiles is well fitted by a single exponential law of the form $I(v) \propto \exp(-|v/v_0|)$, with $v_0 = 4.4$ km s^{-1} for velocities in the range $\approx$−18–0 km s^{-1}. This component dominates the emission between −20 and −8 km s^{-1} in the other CS transitions. Its contribution to each transition can be obtained from a simple scaling to the $J = 7$–6 line profiles. After removing the contribution of this component, an emission excess is observed in the $J = 2$–1, $J = 3$–2 and $J = 5$–4 transitions, which is detected only at velocities between −8 km s^{-1} and +2 km s^{-1}. As shown in Fig. 6, the emission excess is well fitted by a second exponential law $I(v) \propto \exp(-|v/2.5|)$, hence with an exponent different from that of the first CS component. This second component contributes to about half of the total flux emitted in the $J = 2$–1 and $J = 3$–2 (see Section 4 and Table 3). The lower panels in Fig. 5 show the simultaneous two components fit to the line 2–1, 3–2, and 5–4 profiles. Important to note is that the crossing point between the two components shift back and forth from the 2–1 to the 5–4 transition. The latter can in part be due to the higher uncertainties in the fitting of the emission excess, in which we usually have fewer channels than for the first component (see Fig. 6) to make the fit. The uncertainty of the fitted ordinate of this second component is up to ∼23 per cent and therefore close to the intensity contrast between the 2–1 and 3–2 emission of this component (3–2 is about 28 per cent stronger than 2–1). Alternatively, this behaviour can also be due to excitation, in this case with the emission peak of the second component in the 3–2 transition. Finally, weak contamination from the reference position may underestimate the emission close to the ambient velocity, contributing to the apparent shift. Unfortunately, with the present data it is not possible to disentangle between these possibilities. However, due to our method to obtain the fluxes of this second component (Section 4), the above-mentioned uncertainty does not affect significantly the analysis of its emission.

The high signal-to-noise ratio of the line profiles of the $C^{34}S$ $J = 2$–1, $J = 3$–2, and $J = 5$–4 permits a similar analysis of the intensity–velocity distribution. Like for the high-J CS transitions, we find that the $C^{34}S$ (5–4) line profile is well fitted by one single exponential law $I(v) \propto \exp(-|v/4.4|)$. An emission excess is observed between −8 and +2 km s^{-1} in the lower J transitions, which is well fitted by the second exponential law $I(v) \propto \exp(-|v/2.5|)$. Like for CS, the spectral slope of both components in $C^{34}S$ is independent of the transitions considered, which implies excitation conditions independent of the velocity. Therefore, the profile analysis of $C^{34}S$ yields results similar to CS.

Because of the lower signal-to-noise of the data, it was not possible to analyse the intensity–velocity distribution of the CS

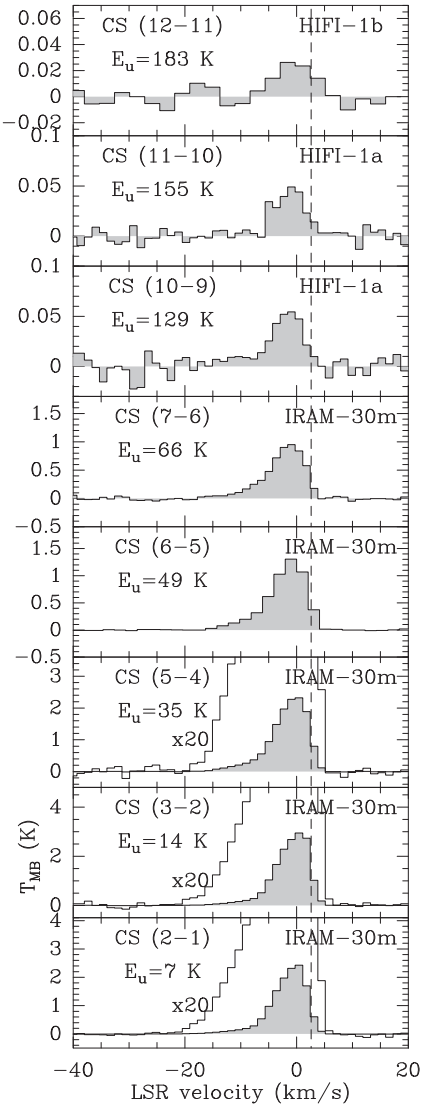

Figure 2. Spectra of the CS main isotope transitions detected by IRAM-30m and *Herschel*-HIFI at L1157-B1. Indicated by labels are the corresponding rotational transition, the upper level energy of the transition (E_u), and the instrument. The three lowest panels also show a zoom in of the wings. The dashed vertical line indicates the cloud V_{sys} of $+2.6\,km\,s^{-1}$ (Bachiller & Perez Gutierrez 1997).

transitions observed in the HIFI range. As discussed in Section 4, the emission of these transitions arises from a region of higher excitation than the $I(v) \propto \exp(-|v/4.4|)$ and $I(v) \propto \exp(-|v/2.5|)$ components observed with the IRAM 30-m telescope.

3.3 Origin of the emission

In Fig. 7, we compare the CS (3–2) profile obtained at the IRAM 30-m telescope with that obtained at the PdBI (Benedettini et al. 2013) when integrating the emission over the region covered by the single-dish main-beam. While the IRAM-30m profile is fitted, as discussed above, with a linear combination of the two exponential components, the spectrum derived from the interferometer is well fitted by the first $\propto \exp(-|v/4.4|)$ component only (convolving the same PdBI map to an even larger beam, Benedettini et al. 2013 also found the first component dominating the 3–2 spectrum). Since most of the high-velocity emission is recovered by the interferometer

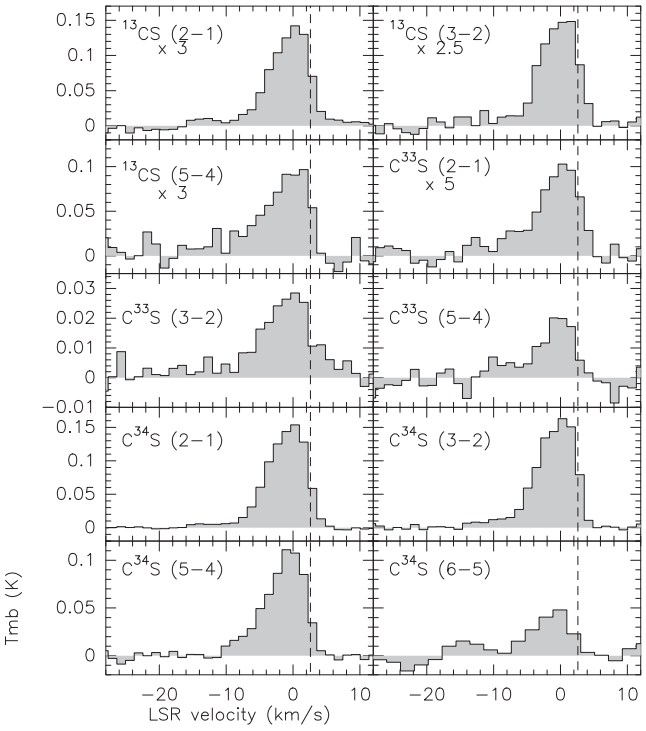

Figure 3. Spectra of the CS isotopologues transitions detected by IRAM-30m at L1157-B1 (in T_{MB} scale). Each panel indicates the corresponding rotational transition. The vertical dashed line indicates the cloud velocity ($V_{sys} = +2.6\,km\,s^{-1}$).

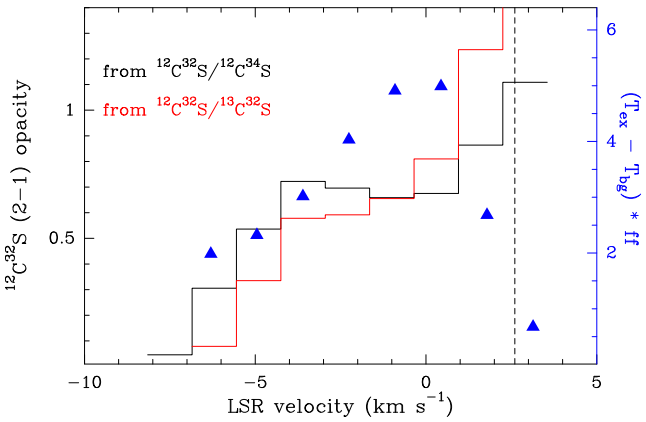

Figure 4. The CS opacity as calculated from the $C^{32}S/C^{34}S$ (2–1) and $^{12}CS/^{13}CS$ (2–1) line ratios (black and red histograms, respectively). Blue triangles show the excitation temperature calculated from opacity (not corrected for beam filling factor, i.e. $(T_{ex}–T_{bg}) \times$ ff). The dashed line indicates the cloud velocity as in Fig. 2 ($V_{sys} = +2.6\,km\,s^{-1}$).

(see Section 3.1), we conclude that the latter map traces the whole emission from the first CS component, and that this emission arises from the walls of the B1 cavity. The size of the first CS component is $\simeq 18$ arcsec, as derived from the PdBI image. We conclude that the low-velocity emission, associated with the $I(v) \propto \exp(-|v/2.5|)$ component is filtered out by the interferometer, suggesting a larger size for this component.

Furthermore, the spectral signatures of the two CS components are found similar (i.e same slope) to those of the components g_2 and g_3 detected in CO by Lefloch et al. (2012), which these authors associated with the B1 and B2 cavities, respectively. As a conclusion,

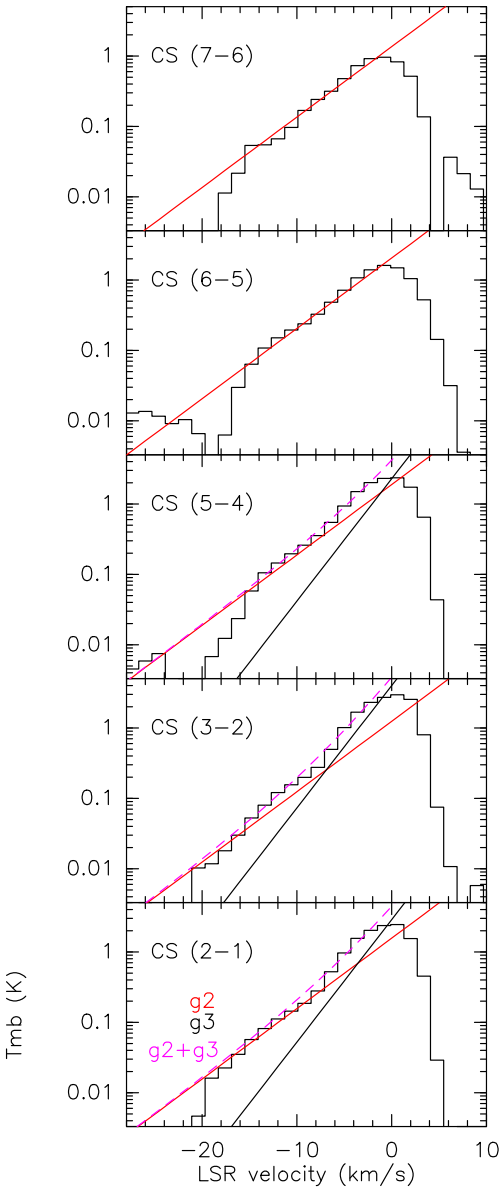

Figure 5. Exponential fits to the CS transitions. The components $I(v) \propto \exp(-|v/4.4|)$ and $I(v) \propto \exp(-|v/2.5|)$ are shown by the red and black lines, respectively; while their linear combination is indicated by the dashed magenta line. These exponential components correspond to the g_2 and g_3 components, respectively, found by Lefloch et al. (2012) in the CO emission.

the emission of the dense gas, as traced by CS and its isotopomers, arise from the outflow cavities associated with B1 and B2. For the sake of consistency with our previous work, in what follows, we will refer to the first and second CS component, respectively, as g_2 and g_3. Also, for consistency with the CO analysis, we will adopt a typical size of 25 arcsec for g_3.

4 PHYSICAL CONDITIONS OF THE GAS

The fluxes used for this analysis are determined as follows.

First, we use the g_2-dominated CS (7–6) line profile to obtain the g_2 contribution to the low-J CS lines. To produce the g_2 profiles, we scaled the CS (7–6) high-velocity intensity to the intensity of the high-velocity emission of the low-J CS transitions. This method

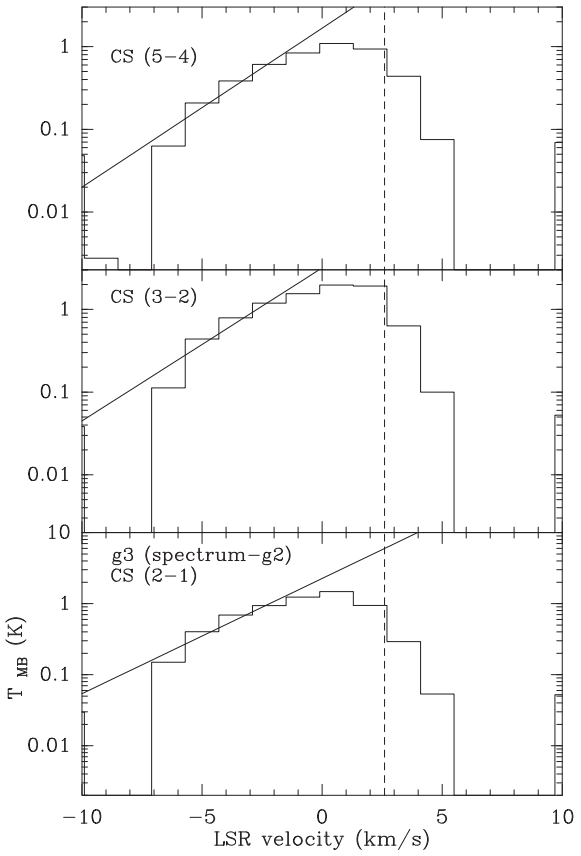

Figure 6. The emission excess, after removing the emission from the first component ($\propto \exp(-|v/4.4|)$). The black line shows the fit of a second exponential component $I(v) \propto \exp(-|v/2.5|)$.

Table 3. CS velocity-integrated intensities of the components g_1, g_2, and g_3, used in the LVG calculations.

Line	HPBW	$\int T_{\rm MB} dv$ (K km s^{-1})$^{(a)}$					
	(arcsec)	$g_1^{(b)}$	$g_2^{(b)}$	$g_3^{(b)}$	$g_1^{(c)}$	$g_2^{(c)}$	$g_3^{(c)}$
			$^{12}C^{32}S$				
2–1	26	–	8.7	8.4	–	10.7	9.9
3–2	17	–	9.8	11.7	–	8.8	11.2
5–4	10	–	13.1	4.9	–	6.0	3.5
6–5	9	–	9.9	–	–	4.3	–
7–6	7	–	8.1	–	–	3.1	–
10–9	44	0.39	–	–	0.64	–	–
11–10	39	0.33	–	–	0.51	–	–
12–11	36	0.28	–	–	0.43	–	–
			$^{12}C^{34}S$				
2–1	26	–	0.37	0.74	–	0.46	0.87
3–2	17	–	0.54	0.61	–	0.49	0.58
5–4	10	–	0.77	–	–	0.35	–
6–5	9	–	0.39	–	–	0.17	–

Notes: $^{(a)}$Obtained from Gaussian fits (see Section 4). $^{(b)}$At the original HPBW. $^{(c)}$Estimated in a 20 arcsec HPBW.

implicitly assumes optically thin emission (as indeed supported by our analysis in Section 3.1) and therefore that the line shape is the same for all the transitions.

Secondly, the g_3 spectra were subsequently produced by subtracting the g_2 spectra from the original low-J CS profiles (i.e. the g_3 component is the residual). The g_2 and g_3 contributions of the $C^{34}S$

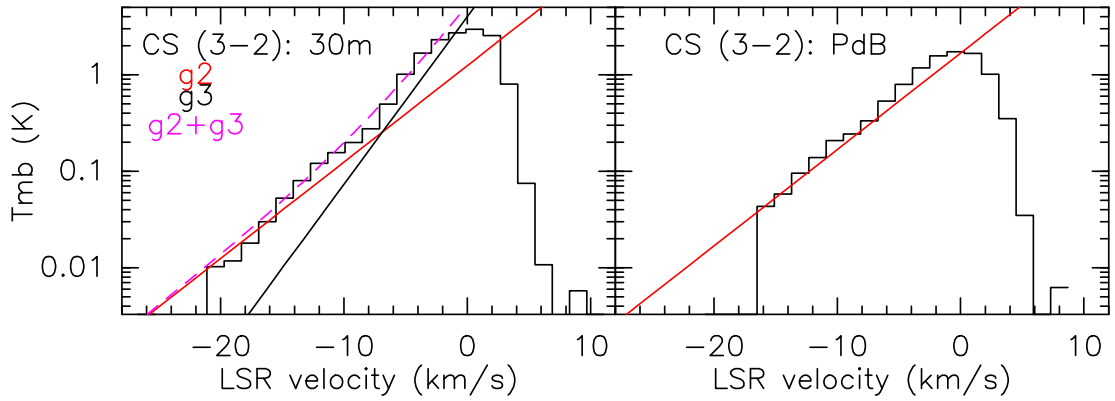

Figure 7. A comparison between the CS (3–2) line profiles at the B1 position, in logarithm scale, as observed with the IRAM-30m (left) and the IRAM-PdBI (right). The PdBI data was convolved to the IRAM-30m angular resolution (17 arcsec). Both panels also show the exponential components that better fit the line profiles. Note how the interferometric data are well fitted with the g_2 component only, while the single-dish data needs both g_2 and g_3 components.

low-J lines were produced in the same way, i.e. scaling to the CS (7–6) profile.

As said above (Section 3.2), the HIFI CS profiles do not have sufficient signal-to-noise ratio to reliable separate them into exponential components. We then take their total integrated flux from Gaussian fits to their profiles. As discussed in Section 4.3, it appears that these transitions arise from a region of much higher excitation than g_2 and g_3, which we tentatively identify with the jet impact shock region, i.e. component g_1 in the terminology of Lefloch et al. (2012). The integrated fluxes of the different components g_1, g_2, and g_3 are reported in Table 3.

We analysed the excitation conditions of the CS line emission with a radiative transfer code in the Large Velocity Gradient (LVG) approach by using the code described in Ceccarelli et al. (2002). We employed the He collisional rates from Lique et al. (2006), and considered 31 levels in the calculations. The model includes the effects of beam filling factor (assuming a source size), and it computes the reduced chi-square (χ^2_r) for each column density, minimizing with respect to kinetic temperature ($T_{\rm kin}$), and H_2 density (n_{H_2}). We adopted a size of 18 arcsec for g_2, as derived from our PdBI map of the CS 3–2 emission, and a typical size of 25 arcsec for g_3. These values are consistent with the sizes estimated from our previous analysis of the CO cavities (Lefloch et al. 2012). The average full width at half-maximum linewidths are 7.0, 7.5, and 5.4 km s^{-1}, for g_1, g_2, and g_3, respectively, and are also used as input in the calculations. The error in the flux measurements considered in the calculations are, taking into account both statistical and calibration uncertainties, about 20 per cent for the low-J CS lines, and up to 30 per cent for the HIFI lines (dominated by noise).

In order to account for beam coupling effects due to the different beam sizes of each transition, we convolved the IRAM-30m CS (3–2) map to different beam sizes and apply a beam coupling correction factor to the measured fluxes of each component. Since the HPBW of the map is 17 arcsec, the beam coupling correction obtained by using the IRAM-30m map can only be applied to the lines with beam sizes larger than this value. The change in the line intensities by convolving the IRAM-30m CS (3–2) map to a 20 arcsec beam is shown in Fig. 8: the ratio between the original and the convolved spectra seems to slightly depend on the velocity, suggesting slightly different emitting sizes (see below). We used the ratios to correct the intensities and to consequently obtain a set of fluxes of the g_2 and g_3 components corrected by beam-coupling effects. The correction factors were taken at +1 km s^{-1} for g_3 (i.e. at a typical velocity

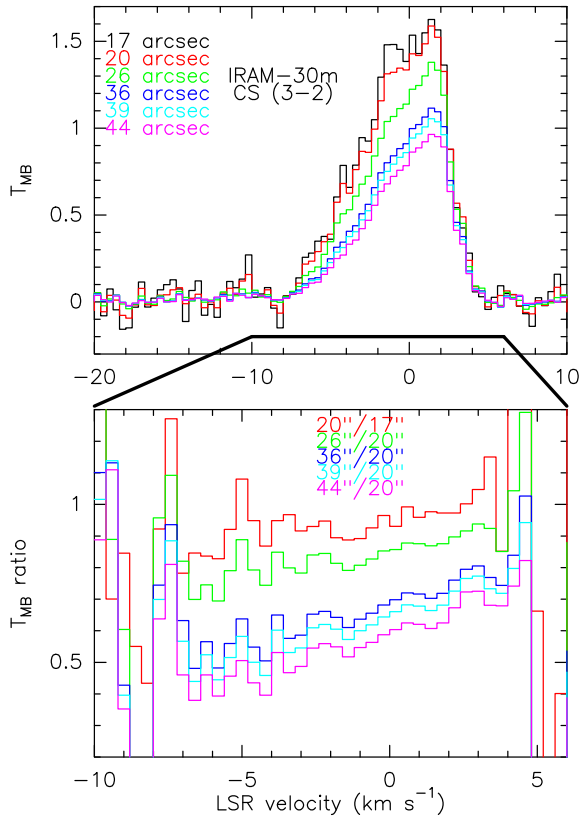

Figure 8. Upper: the resulting CS (3–2) spectra after the convolution of the original IRAM-30m map to different beam sizes. The thick black line shows the velocity range of the lower panel. Lower: the $T_{\rm MB}$ line ratios used to correct for beam coupling in a beam of 20 arcsec. The beam sizes run from smallest at the top to largest at the bottom.

where g_3 emission is brighter than the g_2 one) and at −2 km s^{-1} for g_2. On the other hand, for the mid-J CS lines, i.e. $J = 5$–4, 6–5, and 7–6 lines, whose beam sizes are smaller than 17 arcsec, we used the interferometric CS (3–2) map (synthesized beam ∼3 arcsec), which trace pure g_2 emission (see Fig. 6), to correct their g_2 fluxes from beam coupling effects. To be consistent with the method applied by Lefloch et al. (2012), we used the line intensities as measured in a

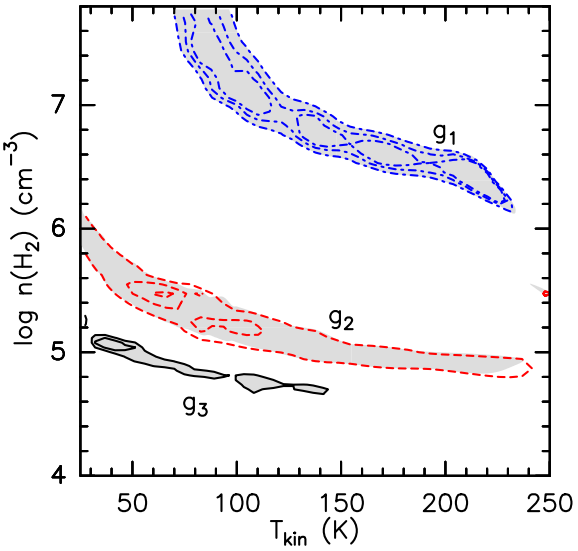

Figure 9. The χ^2_r distribution for the g_1, g_2, and g_3 components (dot–dashed blue, dashed red, and black line, respectively). The valid solution region is delimited by the contour $\chi^2_r = 1$. For g_1 and g_2, χ^2_r contours are 1, 0.5, and 0.2; while for g_3 are 1 and 0.83 (min χ^2_r).

Table 4. Physical parameters constrained by the CS lines.

Component	Size[(a)] (arcsec)	N(CS) (cm^{-2})	n_{H_2} (cm^{-3})
g_1	10	1×10^{13}	$> 10^6$
g_2	18	8×10^{13}	10^5–10^6
g_3	25	8×10^{13}	$0.5–2 \times 10^5$

Note: [(a)]Based on the CS (3–2) interferometric map and CO results (see Sections 3.3 and 4.3).

beam of 20 arcsec. The fluxes of each component with and without the coupling factor corrections are shown in Table 3.

The solutions for the LVG analysis are presented in Fig. 9 as χ^2 plots in the T_{kin} versus n plane. These solutions are discussed here for each component, and the physical conditions constrained by the CS lines are summarized in Table 4.

4.1 The g_3 (L1157-B2) cavity

The g_3 component was analysed using the $J = 2$–1 and 3–2 transitions of the CS and $C^{34}S$ isotopologues. We find valid solutions (i.e. $\chi^2_r = 1$) for source sizes larger than 20 arcsec. Adopting a source size of 25 arcsec (see Section 3.3), the total CS column density is then 8×10^{13} cm^{-2}, and an H_2 volume density in the range of $0.5 - 2 \times 10^5$ cm^{-3} (see Fig. 9). Taking into account the temperature range constrained by CO, 20–30 K (best fit: 23 K; Lefloch et al. 2012), the H_2 volume density of g_3 can be further constrained to $\sim 1 \times 10^5$ cm^{-3}. Using the source-averaged column density N(CO) $= 1 \times 10^{17}$ cm^{-2} (found for g_3 by Lefloch et al. 2012), and assuming [CO]/[H_2] $= 10^{-4}$, we can derive the CS abundance: X(CS) $\simeq 8 \times 10^{-8}$. This value (i) is in agreement with the abundance estimate by Bachiller (2001) and Tafalla et al. (2010), who derived $\sim 10^{-7}$, using the Local Thermodynamic Equilibrium (LTE) approximation, for the low-velocity regime ($-3.5 \leq V \leq +0.5$ km s^{-1}) of the low-J CS emission towards L1157-B1, and (ii) is about one order of magnitude larger than what quoted by Bachiller et al. (2001) towards the position of the driving protostar L1157-mm (3×10^{-9}), thus confirming that the X(CS) can increase in the shocked material located along the cavities.

In addition, we can derive a rough measure of the excitation temperatures from the (T_{ex}–T_{bg}) × ff product derived from the ^{12}CS and ^{13}CS $J = 2$–1 spectra and plotted in Fig. 4. With the assumed size of 25 arcsec, and consequently correcting the $J = 2$–1 emission for the filling factor ff, we have $T_{ex} \simeq 7$–8 K in the –2,0 km s^{-1} range; in other words we find a sub-thermal regime ($T_{kin} \sim 23$ K), consistently with a $J = 2$–1 critical density $\simeq 10^6$ cm^{-3}, which is slightly larger than what found in the LVG analysis (few 10^5 cm^{-3}).

4.2 The g_2 (L1157-B1) cavity

We have first attempted to model the emission of *all* the lines from $J = 2$ to 12, after subtracting the g_3 contribution. We could not find any set of physical conditions (i.e. no valid χ^2) that accounts simultaneously for the low-J CS lines detected with IRAM and those detected with *Herschel* ($J = 10$–9, 11–10, and 12–11). As we show hereafter, we found however that the separate analysis of the IRAM and *Herschel* lines leads to solutions fully consistent with the previous observations of the region.

We have then modelled the low- and mid-J lines detected at millimetre and submillimetre wavelengths, adopting a typical size of 18 arcsec as derived from the interferometric map of the $J = 3$–2 emission. We find column densities of $\sim 8 \times 10^{13}$ cm^{-2} and H_2 volume densities in the range of 10^5–10^6 cm^{-3} (see Fig. 9). These results are fully consistent with the physical conditions in g_2, as derived from CO (Lefloch et al. 2012). Fig. 10 reports the best fit for the spectral line energy distribution for the $C^{32}S$ and $C^{34}S$ emission of g_2 (red line). Taking into account the temperature range constrained by CO, 60–80 K (best fit: 63 K; Lefloch et al. 2012), the density range from CS can be further constrained to ~ 1–5×10^5 cm^{-3}. Using again the source-averaged CO column

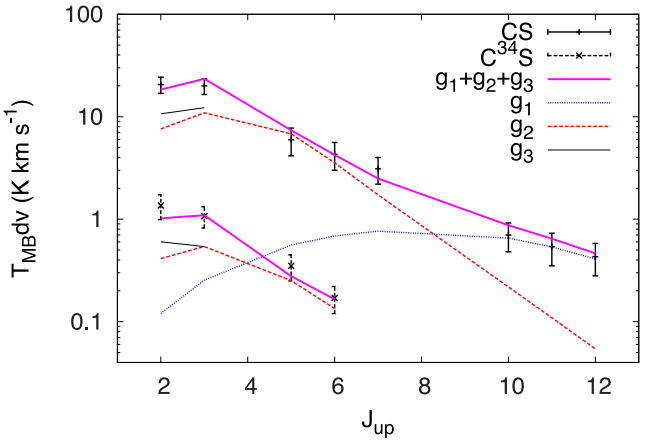

Figure 10. The CS and $C^{34}S$ spectral line energy distribution (data points with error bars) and a three components model with the g_1 (dot–dashed blue line), g_2 (dashed red line), and g_3 (black line) components. The sum of the components is indicated by the thick magenta line. For g_3, assuming a size of 25 arcsec (Lefloch et al. 2012), the best fit gives N(CS) $= 8 \times 10^{13}$ cm^{-2}, $n_{H_2} = 2 \times 10^5$ cm^{-3}, and $T_{kin} = 30$ K. For g_2, assuming a size of 18 arcsec (see Fig. 1), the best fit gives N(CS) $= 8 \times 10^{13}$ cm^{-2}, $n_{H_2} = 2 \times 10^5$ cm^{-3}, and $T_{kin} = 90$ K. For g_1, assuming a size of 10 arcsec (Lefloch et al. 2012; Busquet et al. 2014), the best fit reports N(CS) $= 1 \times 10^{13}$ cm^{-2}, $n_{H_2} = 2 \times 10^7$ cm^{-3}, and $T_{kin} = 90$ K.

density ($\sim 10^{17}$ cm^{-2}), we find a X(CS) of 8×10^{-8} (i.e. similar to that found towards g_3).

We notice, in addition, that the CS column densities and H_2 volume densities for this component is within the range of values reported, based on the analysis of the interferometric CS (2–1) and (3–2) maps, by Benedettini et al. (2013) for some of the high-velocity clumps. In particular, the high-velocity clumps B1a and B1b (both within our beam) are reported with N(CS)= 2–8 $\times$ 10^{13} cm^{-2} and $n_{H_2} = 0.2$–5×10^5 cm^{-3} (table 3 in Benedettini et al. 2013). The similar physical conditions and the fact that the interferometric data alone trace mostly the g_2 component (see Fig. 7) suggest that at least the high-velocity part of the g_2 emission is related with the B1a and B1b clumps.

4.3 The high-excitation CS emission

We analysed separately the flux of the transitions detected with HIFI. We have adopted a typical size of ∼10 arcsec for the emitting region, bearing in mind that the actual size does not influence the density and temperature derived from the LVG modelling provided that the lines are optically thin. Our LVG calculations yield column densities of $\sim 10^{13}$ cm^{-2} and H_2 volume densities $n_{H_2} > 1 \times 10^6$ cm^{-3} (see Fig. 9), and indicates that the three transitions are optically thin.

The analysis of the CO and H_2O line emission in L1157-B1 (Lefloch et al. 2012; Busquet et al. 2014) has shown evidence for a region (with a typical size of ∼10 arcsec) of dense and hot gas ($n_{H_2} > 10^6$ cm^{-3}, < italic > T_k < /italic >≃ 250 K) associated with the impact of the protostellar jet against the B1 cavity. Based on the similarity of the physical conditions, we propose that the high-J CS lines are tracing the jet shock impact region.

Taking into account the constrain on the g_1 kinetic temperature given by the CO and H_2O observations (Lefloch et al. 2012; Busquet et al. 2014) of 200–300 K (best fit: 210 K), the volume density of the g_1 component can be further constrained to 1–5 $\times$ 10^6 cm^{-3}. Fig. 10 reports the best fit for the spectral line energy distribution for the g_1 emission (blue line). According to this model, the integrated low-J CS emission from g_1 would be at least an order of magnitude smaller than the error bars reported for the total CS emission, and two orders of magnitude weaker than the combined g_2 and g_3 contribution. The integrated low-J CS emission from g_1 would then be hidden by the stronger g_2 and g_3 contributions in our data. Also, using the predicted CS (2–1) integrated intensity of g_1, ∼121 mK (Fig. 10), and assuming the intensity–velocity relationship $\propto \exp(-|v/12.5|)$ found in CO for the g_1 component (Lefloch et al. 2012), we can predict the g_1 intensity at the velocities where the g_2 and g_3 emission is not significant in the CS (2–1) spectrum, i.e. < italic > v < /italic >< −20 km s^{-1}. With the relationship obtained, < italic > I(v) < /italic >= 0.012895 ∗ exp(−| < italic > v < /italic > /12.5|), at < italic > v < /italic >= −20 km s^{-1} the expected intensity is ∼2.6 mK (hence <3σ detection limit; see Table 2), making the g_1 component undetectable for < italic > v < /italic >≤ −20 km s^{-1} even in the strongest low-J CS lines.

Comparing with $N(CO) = 1 \times 10^{16}$ cm^{-2}, we derive the CS abundance in g_1 X(CS) ≃ 1×10^{-7}, which is not very different from the values found for g_2 and g_3. The overall X(CS) measurements are consistent with the values found by Tafalla et al. (2010), who analysed the molecular content of two prototypical jet-driven outflows such as L1448 and IRAS 04166+2706, reporting a velocity-dependent CS abundance which increases at most one order of magnitude. In addition, we compared the inferred CS abundances with the prediction made by Podio et al. (2014) by computing the chemical evolution of the gas (from steady-state abundances to enhanced values produced by compression/heating of a shock wave) at the density and temperature of the cavities in L1157-B1. To model the emission of several molecular ions, these authors assumed that the OCS is released from the dust icy mantles due to dust grain sputtering. Their observations are matched by a model in which at the shock age ∼2000–4000 yr the X(OCS) is enhanced up to values ≥ 2×10^{-6}. For their best-fitting model ($X(OCS) = 6 \times 10^{-6}$), the abundance of CS is $\sim 10^{-7}$. This value is in good agreement with the overall CS abundances inferred here.

5 SUMMARY AND CONCLUSIONS

In this paper, we have presented a CS multiline study based on data obtained with *Herschel*-HIFI and IRAM-30m at L1157-B1, within the framework of the CHESS and ASAI surveys. The main results are summarized as follows.

(i) We have detected $^{12}C^{32}S$, $^{12}C^{34}S$, $^{13}C^{32}S$, for a total of 18 transitions, with E_u up to ∼180 K. The unprecedented sensitivity of the survey allows us to carefully analyse the line profiles, revealing high-velocity emission, up to 20 km s^{-1} with respect to the systemic velocity. With the use of the isotopologues, we confirmed that the emission is optically thin at the outflow velocities ($\tau \sim 0.05$ at −7.5 km s^{-1}, while $\tau \sim 1$ at the cloud velocity).

(ii) The profiles can be well fitted by a combination of two exponential laws that are remarkably similar to what previously found using CO. These components have been related to the cavity walls produced by the ∼2000 yr B1 shock (called g_2) and the older (∼4000 yr) B2 shock (g_3), respectively. Previous CO observations allowed us to derive the kinetic temperatures, i.e. 23 K and 64 K for g_3 and g_2, respectively. Using the LVG approximation, we can now put severe constrains on volume density: both the B1 and B2 large cavities are associated with $n_{H_2} \simeq 1$–5×10^5 cm^{-3}. In addition, the high-excitation ($E_u \geq 130$ K) CS lines provide us with the signature of warm (∼200–300 K) and dense ($n_{H_2} = 1$–5×10^6 cm^{-3}) gas, associated with a molecular reformation zone of a dissociative J-type shock (previously detected using [OI], [FeII], CO and H_2O) and expected to arise where the so far unrevealed precessing jet impacts the molecular cavity.

(iii) Our analysis confirms that the CS abundance in shocks increase up to 0.8–1 $\times$ 10^{-7}, i.e. more than one order of magnitude with respect to what is found in the hosting cloud, in agreement with the prediction of the model obtained via the chemical code Astrochem. Such enhancement is possibly due to the release of OCS from dust grain mantles, as suggested by Wakelam et al. (2004), Codella et al. (2005), and, more recently by Podio et al. (2014).

ACKNOWLEDGEMENTS

We thank the anonymous referee for the detailed comments which helped to improve the clarity of this paper. We are grateful to S. Cabrit for useful discussion and suggestions. The Italian authors gratefully acknowledge the support from the Italian Space Agency (ASI) through the contract I/005/011/0, which also provided the fellowships of A.I Gómez-Ruiz and G. Busquet. GB is supported by the Spanish MICINN grant AYA2011-30228-C03-01 (co-funded with FEDER funds). HIFI has been designed and built by a consortium of institutes and university departments from across Europe, Canada and the United States under the leadership of SRON Netherlands Institute for Space Research, Groningen, The Netherlands and with major contributions from Germany, France and the

US. Consortium members are: Canada: CSA, U. Waterloo; France: CESR, LAB, LERMA, IRAM; Germany: KOSMA, MPIfR, MPS; Ireland: NUI Maynooth; Italy: ASI, IFSI-INAF, Osservatorio Astrofisico di Arcetri-INAF; The Netherlands: SRON, TUD; Poland: CAMK, CBK; Spain: Observatorio Astronómico Nacional (IGN), Centro de Astrobiología (CSIC-INTA). Sweden: Chalmers University of Technology - MC2, RSS & GARD; Onsala Space Observatory; Swedish National Space Board, Stockholm University - Stockholm Observatory; Switzerland: ETH Zurich, FHNW; USA: Caltech, JPL, NHSC.

REFERENCES

Bachiller R., Perez Gutierrez M., 1997, ApJ, 487, L93
Bachiller R., Pérez Gutiérrez M., Kumar M. S. N., Tafalla M., 2001, A&A, 372, 899
Benedettini M. et al., 2007, MNRAS, 381, 1127
Benedettini M. et al., 2012, A&A, 539, L3
Benedettini M. et al., 2013, MNRAS, 436, 179
Busquet G. et al., 2014, A&A, 561, A120
Ceccarelli et al., 2010, A&A, 521, L22
Ceccarelli C. et al., 2002, A&A, 383, 603
Chin Y.-N., Henkel C., Whiteoak J. B., Langer N., Churchwell E. B., 1996, A&A, 305, 960
Codella C., Bachiller R., Benedettini M., Caselli P., Viti S., Wakelam V., 2005, MNRAS, 361, 244
Codella C. et al., 2009, A&A, 507, L25
Codella C. et al., 2010, A&A, 518, L112
Codella C. et al., 2012a, ApJ, 744, 164
Codella C. et al., 2012b, ApJ, 757, L9
Codella A., Viti S., Ceccarelli C., Lefloch B., 2013, ApJ, 776, 52
Gómez-Ruiz A., Hirano N., Leurini S., Liu S.-Y., 2013, A&A, 558, 96
Gueth F., Guilloteau S., Bachiller R., 1996, A&A, 307, 891
Gueth F., Guilloteau S., Bachiller R., 1998, A&A, 333, 287
Lefloch B. et al., 2010, A&A, 518, L113
Lefloch B. et al., 2012, ApJ, 757, L25
Looney L. W., Tobin J. J., Kwon W., 2007, ApJ, 670, L131
Müller H. S. P., Schlöder F., Stutzki J., Winnewisser G., 2005, J. Mol. Struct., 742, 215
Neufeld D. A. et al., 2009, ApJ, 706, 170
Nisini B., Giannini T., Neufeld D. A., Yuan Y., Antoniucci S., Bergin E. A., Melnick G. J., 2010, ApJ, 724, 69
Ott S., 2010, in Mizumoto Y., Morita K.-I., Ohishi M., eds, ASP Conf. Ser. Vol. 434, Astronomical Data Analysis Software and Systems XIX. Astron. Soc. Pac., San Francisco, p. 139
Podio L., Lefloch B., Ceccarelli C., Codella C., Bachiller C., 2014, A&A, 565, 64
Tafalla M., Bachiller R., 1995, ApJ, 443, L37
Tafalla M., Santiago-García J., Hacar A., Bachiller R., 2010, A&A, 522, A91
Tobin J. J., Hartmann L., Looney L. W., Chiang H.-F., 2010, ApJ, 712, 1010
van der Tak F. F. S., Black J. H., Schöier F. L., Jansen D. J., van Dishoeck E. F., 2007, A&A, 468, 627
Wakelam V., Caselli P., Ceccarelli C., Herbst E., Castets A., 2004, A&A, 422, 159
Wakelam V., Ceccarelli C., Castets A., Lefloch B., Loinard L., Faure A., Schneider N., Benayoun J.-J., 2005, A&A, 437, 149
Wilson T. L., Rood R., 1994, ARA&A, 32, 191
Zhang Q., Ho P. T. P., Wright M. C. H., Wilner D. J., 1995, ApJ, 451, L71
Zhang Q., Ho P. T. P., Wright M. C. H., 2000, AJ, 119, 1345

This paper has been typeset from a TEX/LATEX file prepared by the author.